

Article

Fe-Substitution for Ni in Misch Metal-Based Superlattice Hydrogen Absorbing Alloys—Part 2. Ni/MH Battery Performance and Failure Mechanisms

Tiejun Meng ¹, Kwo-Hsiung Young ^{1,2,*} , Jean Nei ¹ , John M. Koch ¹ and Shigekazu Yasuoka ³

¹ BASF/Battery Materials-Ovonic, 2983 Waterview Drive, Rochester Hills, MI 48309, USA;
pkumeng@hotmail.com (T.M.); jean.nei@basf.com (J.N.); john.m.koch@basf.com (J.M.K.)

² Department of Chemical Engineering and Materials Science, Wayne State University, Detroit, MI 48202, USA

³ Engineering Division, Ni-MH Group, FDK Corporation, 307-2, Koyagi-Machi, Takasaki, Gunma 370-0042, Japan; shigekazu.yasuoka@fdk.co.jp

* Correspondence: kwo.young@basf.com; Tel.: +1-248-293-7000

Received: 19 July 2017; Accepted: 6 September 2017; Published: 18 September 2017

Abstract: The electrochemical performance and failure mechanisms of Ni/MH batteries made with a series of the Fe-substituted A_2B_7 superlattice alloys as the negative electrodes were investigated. The incorporation of Fe does not lead to improved cell capacity or cycle life at either room or low temperature, although Fe promotes the formation of a favorable Ce_2Ni_7 phase. Fe-substitution was found to inhibit leaching of Al from the metal hydride negative electrode and promote leaching of Co, which could potentially extend the cycle life of the positive electrode. The failure mechanisms of the cycled cells with the Fe-substituted superlattice hydrogen absorbing alloys were analyzed by scanning electron microscopy, energy dispersive spectroscopy and inductively coupled plasma analysis. The failure of cells with Fe-free and low Fe-content alloys is mainly attributed to the pulverization of the metal hydride alloy. Meanwhile, severe oxidation/corrosion of the negative electrode is observed for cells with high Fe-content alloys, resulting in increased internal cell resistance, formation of micro-shortages in the separator and eventual cell failure.

Keywords: metal hydride (MH); nickel/metal hydride (Ni/MH) battery; hydrogen absorbing alloy (HAA); superlattice alloy; failure mechanism

1. Introduction

Misch metal (Mm)-based superlattice hydrogen absorbing alloys (HAAs) exhibit higher capacity, improved high-rate capability, lower self-discharge and wider operating temperature range than the commonly used AB_5 HAA [1,2] in nickel/metal hydride (Ni/MH) batteries. The use of Mm instead of pure La improves the cycle stability [3] and makes superlattice HAAs competitive in the consumer battery market [4]. To further improve the performances of Mm-based superlattice HAAs, the effects of adding Mn [5,6], Co [7,8] and Ce [9] on the structural, gaseous phase and electrochemical hydrogen storage, and full-cell electrochemical performances were investigated. Mn was previously reported to improve high-rate performance, but creates micro-shorts in the separator which results in severe self-discharge. Co improves the low-temperature performance in exchange for self-discharge and high-temperature performance. The use of Ce promotes the AB_2 phase formation and deteriorates the battery performance.

Previously, in the preceding paper (Part 1), the structural, gaseous phase hydrogen storage and electrochemical (in half-cell configuration) hydrogen storage properties of Fe-substituted Mm-based superlattice HAAs have been reported [10]. Fe-substitution promotes the favorable Ce_2Ni_7 (hexagonal) phase and decreases the relatively unfavorable $NdNi_3$ phase. However, the surface catalytic capability—as

reflected by the total volume of surface metallic Ni clusters—was found to decrease with increasing Fe-content. No improvement in discharge capacity was observed and the high rate dischargeability (HRD) of the alloy deteriorated with increasing Fe-content. In this paper (Part 2), the performance and failure mechanisms of Ni/MH batteries made using Fe-substituted HAAs are discussed.

2. Experimental Setup

One hundred C-size Ni/MH batteries using five superlattice HAAs (Fe1 to Fe5) as negative electrode materials were assembled for electrochemical testing. For convenience, Fe1 to Fe5 refer to not only the HAAs, but also the battery cells in this manuscript. The five superlattice HAA ($Mm_{0.83}Mg_{0.17}Ni_{2.94-x}Al_{0.17}Co_{0.2}Fe_x$, $x = 0, 0.05, 0.1, 0.15, 0.2$) powder samples in this study were supplied by Japan Metals and Chemicals Co. (Tokyo, Japan) and their compositions are listed in Table 1. The design formula for all five HAAs is $AB_{3.31}$. Herein, Mm refers to the mixed rare earth metal alloy with a composition of 19.6 wt % La, 40.2 wt % Pr and 40.2 wt % Nd. Structural, gaseous phase hydrogen storage, and the electrochemical properties of the five HAAs were studied and reported in a companion paper (Part 1) [10]. The HAA powder was dry-compacted onto the nickel mesh substrate to form the negative electrode. The positive electrode consists of 94.1 wt % CoOOH-coated $Ni_{0.91}Co_{0.045}Zn_{0.045}(OH)_2$ (~2 wt % CoOOH), 4.9 wt % Co powder and 1 wt % Y_2O_3 additives, and the mixture was wet-pasted onto the nickel foam substrate, dried and then compacted. The Y_2O_3 additive was added due to the ability to increase the open-circuit voltage, decrease the impedance and extend the cycle life [11]. The separator used is Scimat 700/79 acrylic acid grafted polypropylene/polyethylene from the Freudenberg Group (Weinheim, Germany). An aqueous solution consisting of 26.8 wt % NaOH and 1.5 wt % LiOH was used as the electrolyte. The negative to positive capacity ratio was set at 2.0 to maintain a good balance between the overcharge and overdischarge reservoirs [12]. After the cells were sealed, a six-cycle electrochemical formation process was performed using a Maccor Battery Cycler (Tulsa, OK, USA). During the formation process, the cells were charged at a rate of C/10 to 50%, 100% and 120% in the first three cycles and to 150% in the next three cycles. The discharge rate was C/5 for the first five cycles and C/2 for the sixth cycle. The discharge cutoff voltage was 0.9 V.

Table 1. Summary of the compositions and properties of the superlattice hydrogen absorbing alloys (HAAs) used in this study. The gaseous phase maximum hydrogen storage capacity was obtained at 6 MPa hydrogen pressure. The electrochemical capacity was taken from the 2nd cycle at a discharge current of 8 mA g^{-1} with a cutoff voltage of 0.9 V against a standard $Ni(OH)_2$ positive electrode. HRD represents the ratio of the capacity at a discharge current of 200 mA g^{-1} to that at 8 mA g^{-1} . M_S is the saturated magnetic susceptibility, which reflects the total volume of the metallic nickel clusters imbedded in the alloy surface. C is the surface double-layer capacitance obtained from alternative current (AC) impedance measurement.

Alloy	Fe-Content (at%)	Max H Storage Capacity at 30 °C (wt %)	Discharge Capacity at 8 mA g ⁻¹ (mAh g ⁻¹)	Electrochemical to Gaseous Phase Capacity Ratio (%)	HRD (%)	M_S (Memu g ⁻¹)	C (Farad g ⁻¹)
Fe1	0.0	1.43	351	92	93	1016	0.30
Fe2	1.2	1.39	347	93	93	835	0.42
Fe3	2.4	1.37	346	94	94	718	0.37
Fe4	3.6	1.39	335	90	92	481	0.71
Fe5	4.7	1.41	345	91	87	341	0.82

Charge retention was measured using the following procedure. First, the cells were fully charged at a rate of C/10 and discharged at C/5, and the initial discharge capacity was obtained. The cells were then fully charged at C/10 and stored at room temperature (RT) for 7, 14 and 30 days before being discharged at C/5. The remaining capacities after 7, 14 and 30 days were normalized by the initial discharge capacity.

Peak power was measured using the pulse-discharge method. The cells were discharged at C/3 to a 50% depth-of-discharge (DOD) and then discharged using a 30 s pulse at a 2C/3 rate. The voltages at the end of each pulse were recorded and the peak power was calculated [6,8]. The peak power measurements were performed every 50 cycles at 50% DOD until the cells reached the end of their cycle life.

The sealed battery cells were kept in a Blue M Oven (TPS Thermal Power Solutions, White Deer, PA, USA) and tested using a MacCor Battery Cycler. The cell capacity tests were performed at different rates (C/5, C/2, 1C and 2C) and at different temperatures (RT, -10°C and -20°C). The cycle life tests were performed at RT and 50°C through repeated charge/discharge cycling at a rate of C/2. For the cycling tests at RT and 50°C , each charge process was considered complete when the cells reached 105% state-of-charge (calculated based on the initial discharge capacity), and each discharge process achieved a cutoff voltage of 0.9 V. Cycle life ended when the cell capacity dropped below 70% of the initial capacity after the formation process. After cycle life testing at RT, the cells were disassembled for failure mechanism analysis. The remaining electrolyte was removed with a Soxhlet extractor (Thermo Fisher Scientific, Waltham, MA, USA). A JEOL-JSM6320F scanning electron microscope (SEM) with energy dispersive spectroscopy (EDS) capabilities was used to study the morphology and composition of the electrodes after cycling. The solution after etching was analyzed by a Varian Liberty 100 inductively coupled plasma-optical emission spectrometer (ICP, Agilent Technologies, Santa Clara, California, USA).

3. Results and Discussion

3.1. Alloy Properties

Structural, hydrogen storage and electrochemical properties (tested in a flooded half-cell configuration) of the five superlattice HAAs (Fe1 to Fe5) were previously introduced in Part 1 [10] and their capacities (both gaseous phase and electrochemical), HRD, saturated magnetic susceptibility (M_S) and surface double-layer capacitance (C) results are shown in Table 1. Partial substitution of Ni with Fe in Mm-based superlattice HAAs has been shown to increase the abundance of the Ce_2Ni_7 (hexagonal) phase, which is favorable in terms of electrochemical performances [13–15] and decreases the relatively unfavorable NdNi_3 phase. However, the total volume of surface metallic Ni clusters, which reflects the surface catalytic capability [16], decreases with increasing Fe-content (shown in Table 1, M_S decreases dramatically from 1016 memu g^{-1} for Fe1 to 341 memu g^{-1} for Fe5). Consequently, the discharge capacity does not increase and HRD deteriorates with increasing Fe-content in the alloy (shown in Table 1, HRD decreases from 93% for Fe1 to 87% for Fe5 in the half-cell tests). Alloy surface treatment may be a feasible way to overcome this issue [17].

3.2. Cell Capacities at Room Temperature and Low Temperature

Full-cell test results for Fe1 to Fe5 measured at four different rates (C/5, C/2, 1C and 2C) and RT are shown in Figures 1 and 2a shows the cell capacities as a function of the Fe-content of the alloy. At lower rates the five cells exhibit similar capacities; at a discharge rate of C/5, the capacities vary between 4.34 and 4.44 Ah; at a discharge rate of C/2, the capacities decrease to 4.16 to 4.27 Ah. Further increases in discharge rate result in lower capacities and all the samples demonstrate similar capacities at the same rate, except for Fe3 which has the lowest capacities among all alloys. As seen in Table 1, M_S decreases with increasing Fe-content. Consequently, the surface catalytic capability weakens and high-rate performance deteriorates. The low capacities obtained for Fe3, especially at higher rates (1C and 2C), are due to decreased M_S . Although further increases in the Fe-content of the alloy leads to an even smaller M_S , the double-layer capacitance C increases dramatically, indicating the existence of a much larger surface area for the higher Fe-content samples. The large surface area may compensate the loss of surface Ni clusters and lead to comparable capacities obtained at high Fe-content (Fe4 and Fe5).

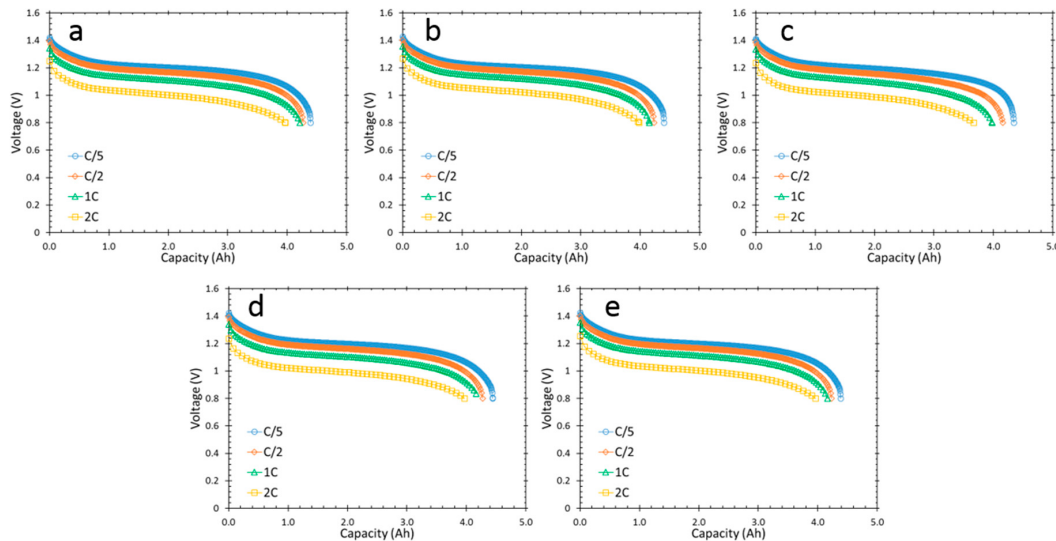


Figure 1. RT discharge voltage curves at four different rates ($C/5$, $C/2$, $1C$ and $2C$) for cells (a) Fe1, (b) Fe2, (c) Fe3, (d) Fe4 and (e) Fe5.

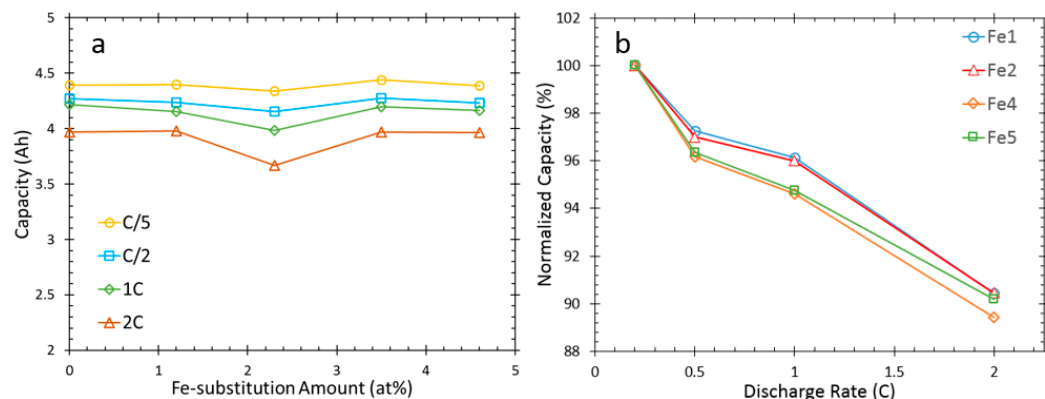


Figure 2. (a) Cell capacities at different rates as functions of the amount of Fe-substitution in the alloy and (b) normalized capacities as functions of discharge rate for cells Fe1, Fe2, Fe4 and Fe5.

It is difficult to establish a correlation between the cell capacity and Fe-content in the alloy from the RT capacity tests. Thus, the normalized capacities are compared in Figure 2b with the focus on the Fe-free (Fe1), low-Fe (Fe2) and high Fe-content alloys (Fe4 and Fe5). The capacities at various rates are normalized for each sample by the capacity at $C/5$. At higher rates above $C/5$, Fe1 and Fe2 demonstrate better rate capability than Fe4 and Fe5.

To further study the effect of the Fe-substitution on rate capability, the cells were tested at low temperatures (LT), specifically $-10\text{ }^{\circ}\text{C}$ and $-20\text{ }^{\circ}\text{C}$. Discharge voltage curves for Fe1, Fe2, Fe4 and Fe5 at $-10\text{ }^{\circ}\text{C}$ and $-20\text{ }^{\circ}\text{C}$ are shown in Figure 3a and b, respectively, and the details of discharge capacity and mid-point voltage are listed in Table 2. A discharge rate of $C/2$ was used for the LT charge/discharge tests. Discharge capacities and mid-point voltages at $-10\text{ }^{\circ}\text{C}$ and $-20\text{ }^{\circ}\text{C}$ for Fe1, Fe2, Fe4 and Fe5 are summarized in Figure 3c. The discharge capacity and mid-point voltage exhibit similar trends, mainly a slight decrease as Fe-content increases to 3.6% (Fe4) followed by a sharp decrease as Fe-content increases to 4.7% (Fe5). Fe5 shows inferior LT electrochemical performance when compared to the Fe-free cell (Fe1), with a 12% lower discharge capacity and a 9% lower mid-point voltage at $-20\text{ }^{\circ}\text{C}$. Higher Fe-content leads to a lower discharge capacity and a lower mid-point discharge voltage, which is consistent with the general trends in AC impedance and magnetic susceptibility measurements reported in Part 1 [10], where RC (the product of charge-transfer

resistance and double-layer capacitance, reflecting the surface catalytic capability) increases and M_s decreases with increasing Fe-content in the alloy. In previous studies, Fe rendered positive and negative influences on the LT performance of AB_2 [18] and AB_5 [19] HAAs, respectively. The impact of the addition of Fe on the LT performance of A_2B_7 HAA is closer to that of AB_5 HAA.

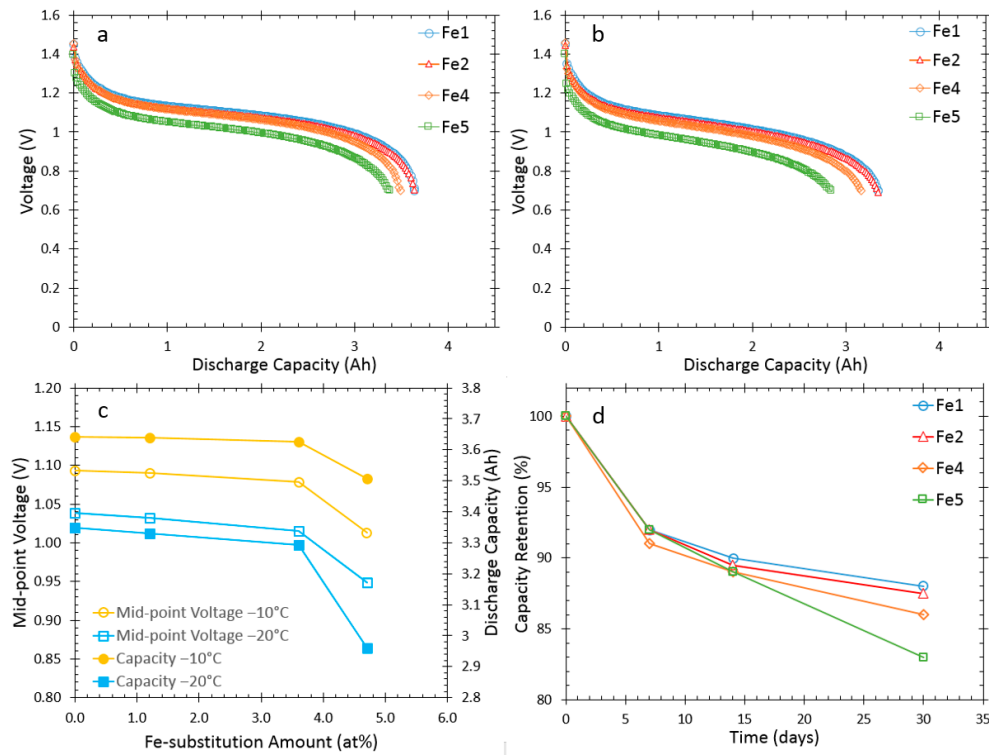


Figure 3. The discharge voltage curves obtained using a rate of C/2 at (a) $-10\text{ }^{\circ}\text{C}$ and (b) $-20\text{ }^{\circ}\text{C}$; (c) a summary of the discharge capacity and mid-point voltage at $-10\text{ }^{\circ}\text{C}$ and $-20\text{ }^{\circ}\text{C}$; and (d) 30-day capacity retention at RT for cells Fe1, Fe2, Fe4 and Fe5.

Table 2. Summary of discharge capacities at different rates and temperatures, mid-point voltages at different temperatures and 30-day charge retention. $Q_{C/2}$ and Q_{2C} are the discharge capacities measured at C/2 and 2C, respectively.

Alloy	$Q_{C/2}$ at RT (Ah)	Q_{2C} at $20\text{ }^{\circ}\text{C}$ (Ah)	$Q_{C/2}$ at $-10\text{ }^{\circ}\text{C}$ (Ah)	$Q_{C/2}$ at $-20\text{ }^{\circ}\text{C}$ (Ah)	30-day Charge Retention (%)	Mid-Point Voltage at $-10\text{ }^{\circ}\text{C}$ (V)	Mid-Point Voltage at $-20\text{ }^{\circ}\text{C}$ (V)
Fe1	4.27	3.97	3.64	3.35	88	1.093	1.038
Fe2	4.27	3.97	3.63	3.34	87	1.090	1.032
Fe4	4.27	3.97	3.62	3.29	86	1.079	1.015
Fe5	4.23	3.96	3.51	2.96	83	1.013	0.949

Charge retention tests for Fe1, Fe2, Fe4 and Fe5 were performed at RT at the end of days 7, 14 and 30, and the results are shown in Figure 3d. The charge/discharge rate used for the tests was C/5 and the capacities have been normalized by the original capacity. Cells Fe4 and Fe5, with higher Fe-content, exhibited lower capacity retention than Fe1 and Fe2 after 14 days. At the end of 30 days, capacity retention followed the trend of Fe1 (88%) > Fe2 (87%) > Fe4 (86%) > Fe5 (83%). Capacity retention properties of the Mn- or Co-substituted superlattice HAAs were studied previously. The capacity loss observed in the Mn-substituted HAAs was attributed to micro-shortages between the positive and negative electrodes caused by oxides of Mn and Zn [20]. For the Co-substituted HAAs, the high corrosion rate of Co in the alkaline electrolyte resulted in capacity loss [21]. The alloys in this study were designed based on a Co-containing superlattice HAA, and Fe1 has the same composition as C3 in [21]. The lower charge retention for cells with high Fe-content HAAs indicates

that, other than the corrosion of Co, there are other factors causing further reduction in capacity after storage. More severe oxidation in the Fe containing alloys may have a role in capacity loss as well, which was observed by SEM/EDS and will be presented in the failure analysis section. Fe improved the charge retention properties of AB_2 [18] HAAs and deteriorated those of AB_5 [19] HAAs. Similar to LT performance, the effects of Fe for A_2B_7 HAA are similar to those for AB_5 HAA with regard to charge retention performance.

3.3. Cycle Life and Peak Power

Cycle life performances of cells Fe1 to Fe5 were measured at RT and 50 °C. Results are shown in Figure 4 and summarized in Table 3. The charge processes were terminated when the cells reached 105% state-of-charge (calculated based on the initial discharge capacity) and the discharge process was finished at a cutoff voltage of 0.9 V. A rate of C/2 was used for both the charge and discharge processes. At RT, the Fe-free cell (Fe1) showed the highest cycle life—1055 cycles. Cycle life decreases dramatically with increasing Fe-content. Fe2 contained 1.2 at% Fe and demonstrated a cycle life of 720. When the Fe-content increased to 2.4 at% (Fe3) and above (Fe4 and Fe5), cycle life dropped to approximately 400 cycles. At 50 °C, the cycle life performances of all cells were greatly reduced, but exhibited a similar trend increasing Fe-content in the alloy. Fe1 showed a cycle life of 345, while cells with high Fe-content HAAs (Fe3, Fe4 and Fe5) demonstrated cycle numbers of less than 200. The accelerated capacity degradation at a temperature above 50 °C is common for HAA and can be attributed to higher degrees of oxidation, leaching and poisoning of the positive electrode [22,23]. The rapid deterioration in cycle life caused by increasing Fe-content in A_2B_7 HAAs was seen previously in AB_5 HAAs [19].

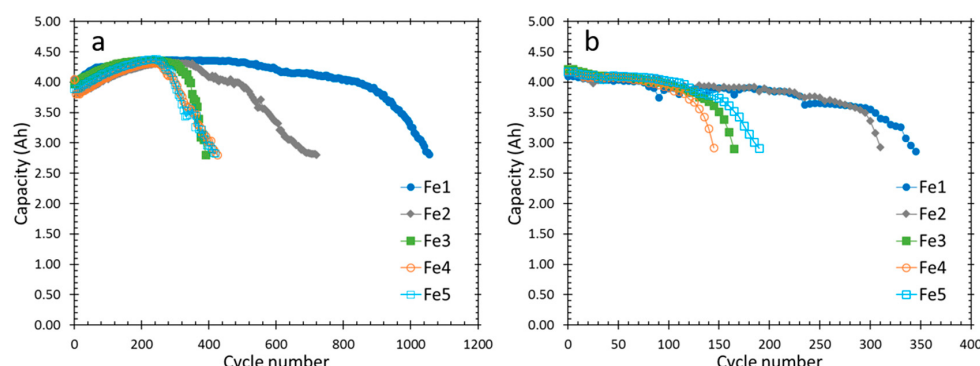


Figure 4. Cycle life performances of cells Fe1 to Fe5 measured at (a) RT and (b) 50 °C at a charge/discharge rate of C/2.

Table 3. Cycle life and peak power performances for cells Fe1 to Fe5. The cycle life tests were performed at RT and 50 °C, at a charge/discharge rate of C/2. Peak power was measured at 50% depth-of-discharge (DOD).

Alloy	Cycle life at C/2, RT	Cycle life at C/2, 50 °C	Initial Peak Power at 50% DOD (W kg^{-1})	Cycle Life (Peak Power Reached 100 W kg^{-1})
Fe1	1055	345	192	550
Fe2	720	310	195	450
Fe3	390	165	190	450
Fe4	425	145	179	450
Fe5	420	190	181	450

The peak power of cells Fe1 to Fe5 was measured every 50 cycles at 50% DOD and RT. The results are shown in Figure 5 and the initial peak power data is listed in Table 3. Details of the testing method can be found in our previous studies on Mn- and Co-substitutions in A_2B_7 [6,8]. During early cycling, cells with high Fe-content HAAs (Fe4 and Fe5) show lower peak power values than those with the Fe-free

(Fe1) and low Fe-content HAAs (Fe2 and Fe3). After 200 cycles, there was a clear trend as the peak power first decreases and then increases as Fe-content increases, with Fe3 showing the lowest peak power. Fe1 demonstrates the best power stability among all the tested cells, which was consistent with its superior cycle stability (Figure 4). The trend of peak power change with the Fe-content was consistent with the findings regarding RT rate capability (Figure 2a), since the peak power also depends on surface catalytic capability and the surface area of the HAA. Fe3 has a much lower amount of catalytic Ni clusters compared to Fe1 and a much smaller surface area than Fe4 and Fe5, which results in its low peak power.

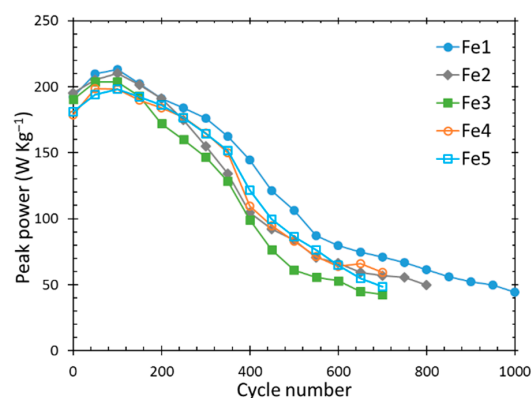


Figure 5. Peak power for cells Fe1 to Fe5 measured at 50% DOD and RT.

3.4. Failure Analysis

After cycle life tests, the cells were taken apart and their failure modes were studied by SEM, EDS and ICP. SEM backscattered electron images (BEIs) of the positive electrodes from cells Fe1 to Fe5 cycled at RT are shown in Figure 6. EDS was performed to measure the average chemical composition across a clean region without Ni foam, at 1000× magnification. The chemical compositions of the cycled positive electrodes were measured by EDS and are listed in Table 4.

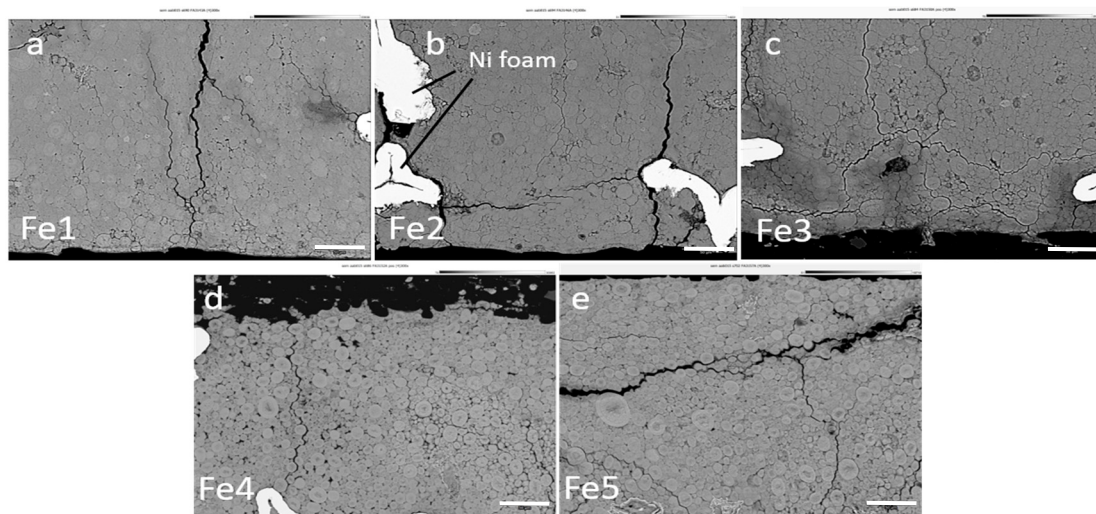


Figure 6. SEM micrographs of the positive electrodes of cells (a) Fe1, (b) Fe2, (c) Fe3, (d) Fe4 and (e) Fe5 after cycle life testing at RT. Magnification: 300×. The scale bar (white) represents 50 μ m. The bright white regions in (b–d) are the Ni-foam current collectors.

Table 4. Chemical compositions (at%) measured by EDS of the positive electrodes after cycle life testing at RT.

Cell	Ni	Co	Zn	Al
Fe1	76.5	18.0	2.3	3.2
Fe2	75.7	18.5	2.6	3.2
Fe3	76.6	18.0	2.8	2.6
Fe4	74.9	20.2	2.7	2.2
Fe5	75.1	20.2	2.6	2.1

The most noticeable composition changes in the positive electrodes include the decrease in Al content and increase of Co content as the Fe-content in the alloy increases. The original positive electrode is Al free and the only Al source in the cell is the negative electrode. It has been reported that Al can leach from Co substituted superlattice HAAs and higher Co contents result in a higher degree of Al leaching [8]. However, Al is essential to superlattice HAA due to the ability to stabilize the structure against amorphization [24]. The alloys in this study contain 4.7 to 4.8 at% Co, which contributes to a high Al content (3.2 at%) in the cycled positive electrode of the cell with the Fe-free alloy (Fe1). As the Fe-content of the alloy in the negative electrode increases, the Al content in the heavily cycled positive electrode decreases to 2.1 at% for Fe5. Meanwhile, the Co content in the positive electrode increases from 18.0% to 20.2%. Therefore, Fe-substitution inhibits the leaching of Al from the superlattice HAA, but promotes the leaching of Co from the same place. Since the evolution of the Al and Co leaching are inversely correlated with the Fe-content, they eliminate the possibility of linking higher Al content to higher cycle number in cells with low Fe-content HAAs. Moreover, it is well known that the addition of Al in the positive electrode promotes the formation of α -Ni(OH)₂, which has a higher specific capacity than the initial β -Ni(OH)₂ [25]. However, the volume expansion caused by the β to α phase change leads to the swelling of the positive electrode [26]. Upon cycling, the developed stress may cause cracking and pulverization, which will eventually terminate cell activity. This is the reason α -Ni(OH)₂ inhibitors, such as Zn or Cd, are added to ensure a long cycle life [27–30]. Since Fe-substitution can inhibit leaching of Al from the negative electrode and, in turn, the formation of α -Ni(OH)₂, higher Fe-content is ideally beneficial to cycle life performance. However, the cycle life test presents the opposite result, specifically higher Fe-content leads to shorter cycle life. Furthermore, the SEM micrographs in Figure 6 show that the spherical Ni(OH)₂ particles are in good shape for all cycled samples and no obvious swelling or pulverization is observed. The effects of Al leaching from the negative electrodes is not observed. Therefore, it is unlikely that the shortened cycle life of Fe3 to Fe5 is caused by the degradation of the positive electrode.

The chemical compositions of the cycled negative electrodes were measured using ICP and the data is listed in Table 5. After cycle testing at RT, the composition of each negative electrode does not change significantly compared to that of the original HAA powder (data shown in Table 1 in Part 1) except that the Al content in all the samples decreases by nearly 1%, which results in a corresponding increase in Al in the positive electrodes. The increase of the Fe-content and decrease of the Ni content from Fe1 to Fe5 occur by alloy design. The SEM BEI micrographs of the cycled negative electrodes from cells Fe1 to Fe5 are shown in Figure 7. The cycled Fe1 (Figure 7a) exhibits severe pulverization and the HAA particles break into smaller pieces and gradually lose electrical connections to the current collector, which is a common failure mode for Ni/MH batteries [22,31,32]. Fe2 also suffers from severe pulverization, as shown in Figure 7b. In addition, the large darker grey colored area indicates that oxidation occurs around the pulverized HAA particles, which was confirmed by spot EDS measurements. The oxygen content in the grey area varies between 34 to 54 at%, as measured by EDS. Fe3 to Fe5 exhibit much shorter cycle life performances than Fe1, and their SEM BEI micrographs (Figure 7c–e) do not show signs of severe pulverization. The large HAA chunks do not appear to break into pieces and still occupy the largest portion of the surfaces. Instead, the large grey areas observed in Fe3 to Fe5 suggest severe oxidation, which was also confirmed by EDS measurements.

For Fe5, the grey area occupies the majority of the image, indicating that severe oxidation occurred in all the samples. Pressure-composition-temperature (PCT) hysteresis, a strong indicator for the inclination for HAA pulverization [33], for this series of alloys [10] does not support the direct link of degree-of-pulverization to the Fe-content. The heavy pulverization found in cells with Fe-free or low-Fe-content HAAs is due to the large number of cycles.

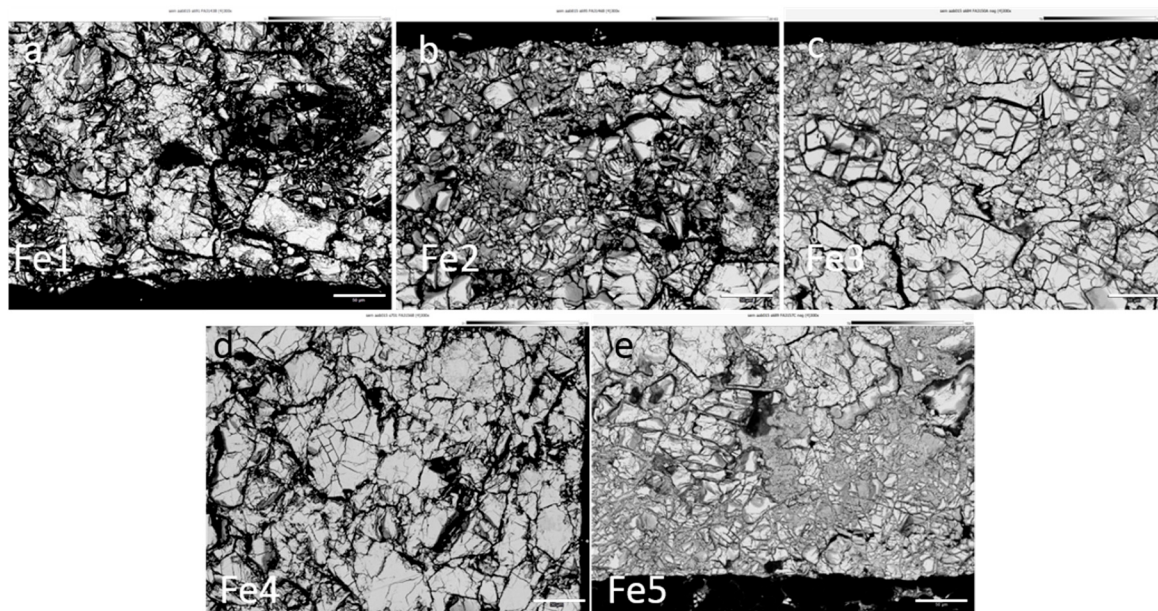


Figure 7. SEM micrographs of the negative electrodes of cells (a) Fe1, (b) Fe2, (c) Fe3, (d) Fe4 and (e) Fe5 after cycle life testing at RT. The scale bar represents 50 μm .

Table 5. Chemical compositions (at%), determined by ICP, of the negative electrodes after cycle life testing.

Cell	Mn	Ni	Co	Mg	Al	Fe
Fe1	19.1	69.5	4.6	3.7	3.1	0.0
Fe2	18.5	68.3	4.9	3.7	3.2	1.4
Fe3	19.2	66.7	4.6	3.8	3.3	2.4
Fe4	18.6	66.0	5.1	3.7	3.2	3.5
Fe5	19.2	64.3	4.6	3.8	3.0	5.1

SEM/EDS analyses were used to study the cross-section of the positive electrode/separator/negative electrode sandwich structure of the heavily oxidized Fe3 to Fe5 after cycle life testing at RT. The SEM BEI micrographs are shown in Figure 8a–c and their corresponding oxygen-EDS (O-EDS) micrographs are presented in Figure 8d–f. Each figure, from top to bottom of the sandwich, consists of the negative electrode, separator and positive electrode. The O-EDS mappings for Fe3 and Fe4 indicate that the oxidation of the negative electrode occurs mainly around the particle/grain boundaries, while Fe5—which has the highest Fe-content—exhibits a heavily oxidized surface across the negative electrode. This finding is consistent with the SEM BEI study above, confirming that the cell failure is caused by severe oxidation instead of pulverization with increasing Fe-content in HAAs. A heavily oxidized surface layer increases the internal resistance of the cell and leads to a shorter cycle life.

The cells after cycle life testing at 50 °C were also taken apart and investigated by SEM/EDS. Cycle life performance decreases dramatically with increasing temperature. In addition, the failure modes are similar. As shown in Figure 9, cells with the Fe-free (Fe1) and low-Fe-content (Fe2) HAAs show significant pulverization at the negative electrodes during the end of cycle life, which is the main cause of cell failure. When the Fe-content increases above 1.2 at% (Fe3 to Fe5), oxidation at the

HAA surfaces becomes more significant (Figure 9c–e). Fe5 exhibits the most severe oxidation among all alloys. Figure 10 shows the SEM BEI micrographs of the cross-sections and their corresponding O-EDS mappings for Fe2 to Fe5. O-EDS mapping does not show a significant oxygen level in the cycled negative electrode in cell Fe2, which indicates that oxidation should be excluded as the main cause of cell failure. For Fe3 to Fe5, the negative electrodes are severely oxidized, whereas no obvious pulverization is observed. In addition to negative electrode oxidation, the separators in Fe3 to Fe5 are squeezed by the expansion in the positive electrode and debris/deposits are found in the separators, which is attributed to electrolyte dry-out. Electrolyte dry-out is another typical failure mode and caused cell failure of the Co-substituted HAA cells tested at 50 °C. EDS measurements show that the debris/deposits contain Ni, Co, Mg and Al (mainly Ni and Co), which originated from the corroded negative electrode and formed a micro-shortage network that is detrimental to cycle life performance. Such debris/deposits were also observed in the high Fe-content cells Fe4 and Fe5 after cycling at RT.

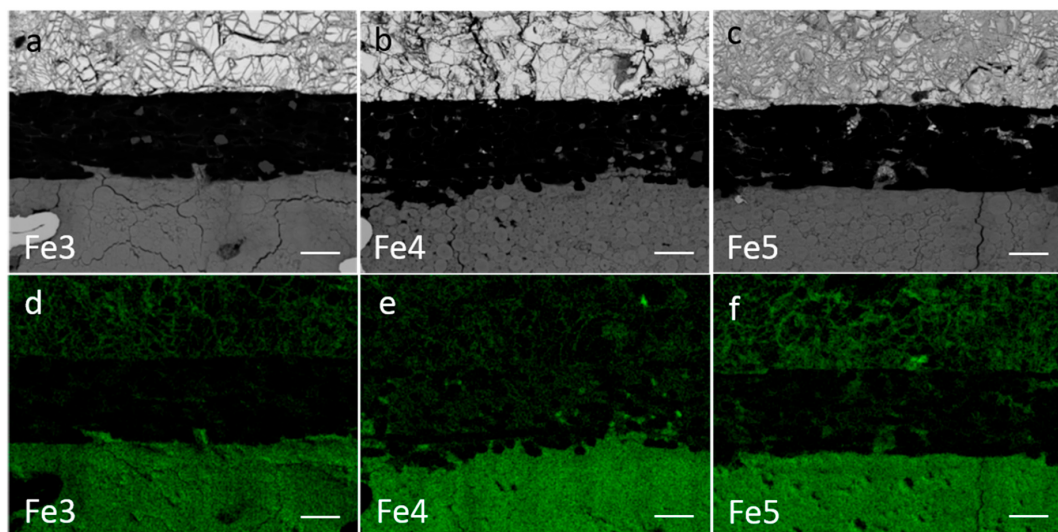


Figure 8. SEM micrographs of the cross-sections of cells (a) Fe3, (b) Fe4 and (c) Fe5 and their corresponding O-EDS elemental mappings (d) Fe3, (e) Fe4 and (f) Fe5 after cycle life testing at RT. The scale bar represents 50 μ m. In each figure, the sandwich structure from top to bottom consists of the negative electrode, separator and positive electrode.

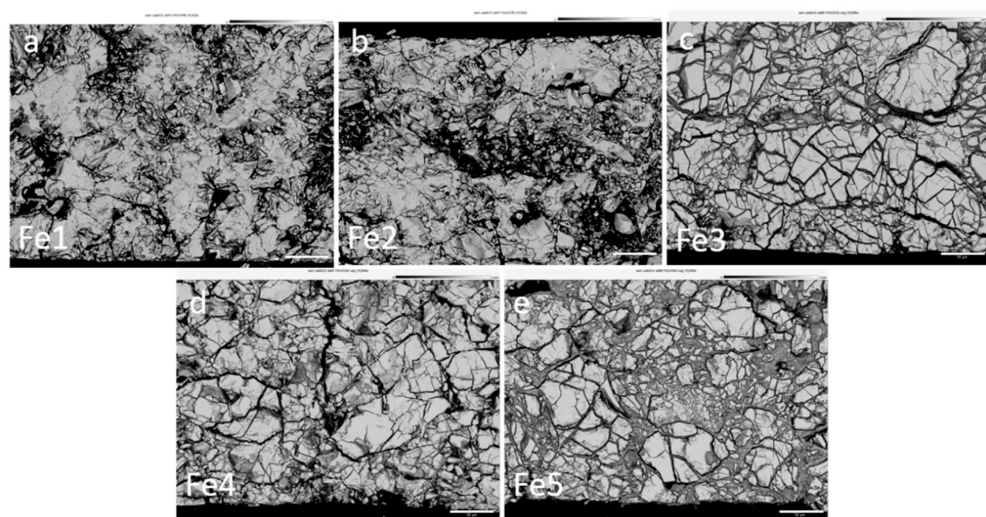


Figure 9. SEM micrographs of the negative electrodes of cells (a) Fe1, (b) Fe2, (c) Fe3, (d) Fe4 and (e) Fe5 after cycle life testing at 50 °C. The scale bar represents 50 μ m.

The cells cycled at RT and 50 °C show similar failure mechanisms. Cells with Fe-free and low-Fe-content HAAs demonstrate long cycle life and eventually fail due to pulverization/disintegration of the negative electrode. With increasing Fe-content in HAAs, oxidation/corrosion of the negative electrode dominates and has two negative influences. First, surface oxidation may lead to increased internal resistance and deterioration of the cell capacity and cycle life. Second, during the oxidation/corrosion of HAAs, Ni, Co or other elements may leach from the negative electrode and deposit on the separator. Such deposits/debris may eventually develop into a micro-shortage network and therefore reduce cell capacity, cycle life and shelf life.

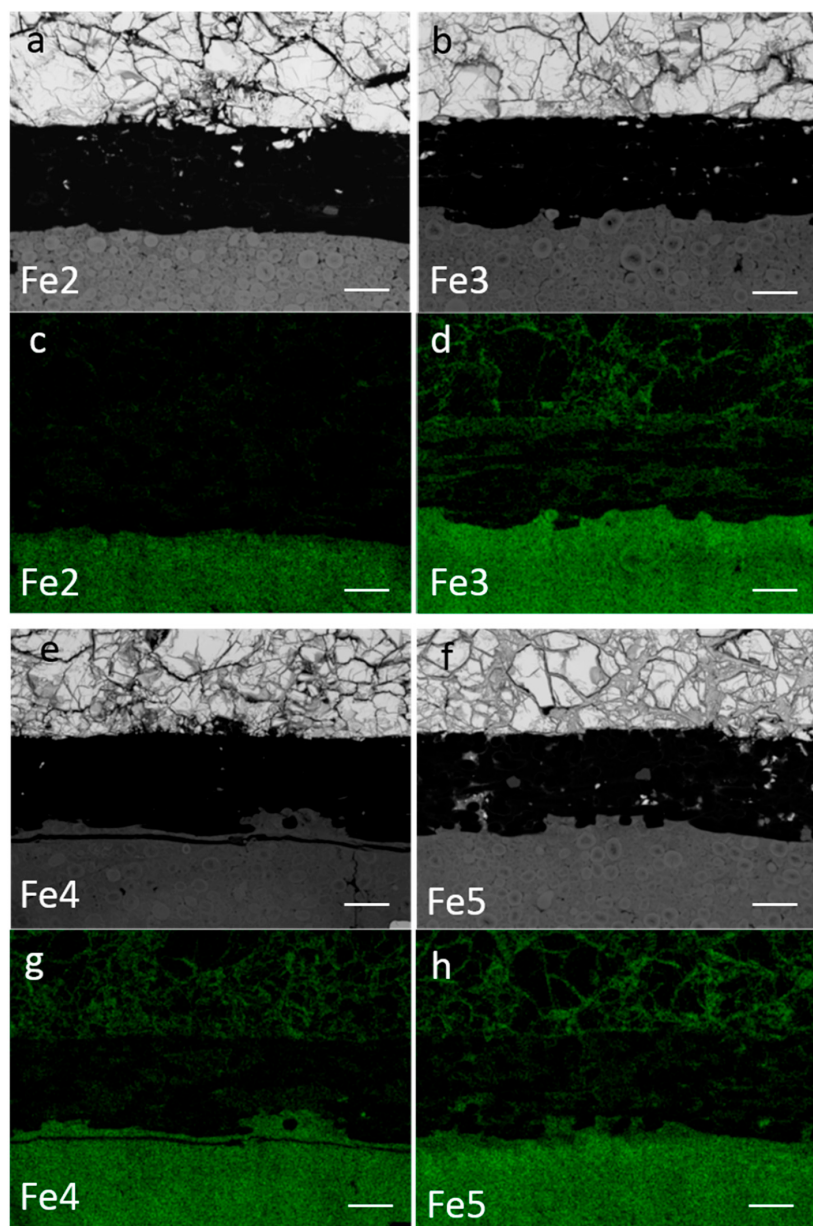


Figure 10. SEM micrographs of the cross-sections of cells (a) Fe2, (b) Fe3, (e) Fe4, and (f) Fe5 and their corresponding O-EDS elemental mappings of cells (c) Fe2, (d) Fe3, (g) Fe4 and (h) Fe5 after cycle life testing at 50 °C. The scale bar represents 50 μ m. In each figure, the sandwich structure from top to bottom consists of the negative electrode, separator and positive electrode.

4. Conclusions

The effects of the Fe-substitution in Mm-based superlattice alloys on the performances of nickel/metal hydride batteries and their failure mechanisms were studied in Part 2 of this paper.

Due to the complexity involved with the Fe-substitution and limited number of compositions selected, the variations in some properties are not very smooth; however, general trends are still observable and reported. Although the incorporation of Fe promotes the formation of a favorable Ce_2Ni_7 phase, the full-cell capacities at room temperature, $-10\text{ }^\circ\text{C}$ and $-20\text{ }^\circ\text{C}$, cycle life performances at room temperature and $50\text{ }^\circ\text{C}$, capacity retention, mid-point discharge voltage and peak power all deteriorate with increasing Fe-content, especially in samples with high Fe-content. Fe in the alloy also inhibits leaching and migration of Al from the negative electrode to the positive electrode, while facilitating the leaching of Co from the negative electrode. However, the cycle life performance was dominated by the negative electrode in this study. Cells with high Fe-content alloys show much lower room temperature and $50\text{ }^\circ\text{C}$ cycle life performances and peak power than those with Fe-free (Fe1) and low Fe-content (Fe2) alloys. The failure of cells Fe1 and Fe2 is mainly attributed to the pulverization of the negative electrode, while cells with high Fe-content HAAs (Fe3 to Fe5) suffer from severe oxidation/corrosion of the negative electrode, which greatly limits cycle life performance at room temperature and $50\text{ }^\circ\text{C}$.

Acknowledgments: The authors would like to thank their coworkers at BASF-Ovonic: David A. Pawlik, Alan Chan and Ryan J. Blankenship for their help on material characterizations, and Sui-ling Chen, Cheryl Setterington and Nathan English for battery measurements.

Author Contributions: Tiejun Meng designed the experiments and analyzed the results. Kwo-Hsiung Young interpreted the data. Jean Nei prepared the electrode samples and conducted the magnetic measurements. John M. Koch prepared samples for failure analysis. Shigekazu Yasuoka designed and obtained the test samples.

Conflicts of Interest: The authors declare no conflict of interest.

Abbreviations

Mm	Misch metal
HAA	Hydrogen absorbing alloy
Ni/MH	Nickel/metal hydride
HRD	High-rate dischargeability
RT	Room temperature
DOD	Depth-of-discharge
SEM	Scanning electron microscope
EDS	Energy dispersive spectroscopy
M_s	Saturated magnetic susceptibility
C	Double-layer capacitance
LT	Low temperature
R	Charge-transfer resistance
BEI	Backscattered electron images
PCT	Pressure-composition-temperature
O-EDS	Oxygen-energy dispersive spectroscopy

References

- Yasuoka, S.; Magari, Y.; Murata, T.; Tanaka, T.; Ishida, J.; Nakamura, H.; Nohma, T.; Kihara, M.; Baba, Y.; Teraoka, H. Development of high-capacity nickel-metal hydride batteries using superlattice hydrogen-absorbing alloys. *J. Power Sources* **2006**, *156*, 662–666.
- Takasaki, T.; Nishimura, K.; Saito, M.; Fukunaga, H.; Iwaki, T.; Sakai, T. Cobalt-free nickel-metal hydride battery for industrial applications. *J. Alloy. Compd.* **2013**, *580*, S378–S381.

3. Liu, J.; Han, S.; Li, Y.; Yang, S.; Chen, X.; We, C.; Ma, C. Effect of Pr on phase structure and cycling stability of La-Mg-Ni-based alloys with A_2B_7 - and A_5B_{19} -type superlattice structure. *Electrochim. Acta* **2015**, *184*, 257–263.
4. Kai, T.; Ishida, J.; Yasuoka, S.; Takeno, K. The effect of nickel-metal hydride battery's characteristics with structure of the alloy. In Proceedings of the 54th Battery Symposium in Japan, Osaka, Japan, 7–9 October 2013.
5. Young, K.; Wong, D.F.; Wang, L.; Nei, J.; Ouchi, T.; Yasuoka, S. Mn in misch-metal based superlattice metal hydride alloy—Part 1 Structural, hydrogen storage and electrochemical properties. *J. Power Sources* **2015**, *277*, 426–432.
6. Young, K.; Wong, D.F.; Wang, L.; Nei, J.; Ouchi, T.; Yasuoka, S. Mn in misch-metal based superlattice metal hydride alloy—Part 2 Ni/MH battery performance and failure mechanism. *J. Power Sources* **2015**, *277*, 433–442.
7. Wang, L.; Young, K.; Meng, T.; Ouchi, T.; Yasuoka, S. Partial substitution of cobalt for nickel in mixed rare earth metal based superlattice hydrogen absorbing alloy—Part 1 Structural, hydrogen storage and electrochemical properties. *J. Alloy. Compd.* **2016**, *660*, 407–415.
8. Wang, L.; Young, K.; Meng, T.; English, N.; Yasuoka, S. Partial substitution of cobalt for nickel in mixed rare earth metal based superlattice hydrogen absorbing alloy—Part 2 Battery performance and failure mechanism. *J. Alloy. Compd.* **2016**, *664*, 417–427.
9. Yasuoka, S.; Ishida, J.; Kichida, K.; Iniu, H. Effects of cerium on the hydrogen absorption-desorption properties of rare Earth-Mg-Ni hydrogen-absorbing alloys. *J. Power Sources* **2017**, *346*, 56–62.
10. Young, K.; Ouchi, T.; Nei, J.; Yasuoka, S. Fe-substitution for Ni in misch metal-based superlattice hydrogen absorbing alloys—Part 1 Structural, hydrogen storage, and electrochemical properties. *Batteries* **2016**, *2*, 34.
11. Kong, L.; Chen, B.; Young, K.; Koch, J.; Chan, A.; Li, W. Effects of Al- and Mn-contents in the negative MH alloy on the self-discharge and long-term storage properties of Ni/MH battery. *J. Power Sources* **2013**, *213*, 128–139.
12. Young, K.; Wu, A.; Qiu, Z.; Tan, J.; Mays, W. Effects of H_2O_2 addition to the cell balance and self-discharge of Ni/MH batteries with AB_5 and A_2B_7 alloys. *Int. J. Hydrot. Energy* **2012**, *37*, 9882–9891.
13. Young, K.; Yasuoka, S. Past, Present, and Future of Metal Hydride Alloys in Nickel-Metal Hydride Batteries. In Proceedings of the 14th International Symposium on Metal-Hydrogen Systems, Manchester, UK, 21–25 July 2014.
14. Yan, H.; Xiong, W.; Wang, L.; Li, B.; Li, J.; Zhao, X. Investigations on AB_3 -, A_2B_7 - and A_5B_{19} -type La-Y-Ni system hydrogen storage alloys. *Int. J. Hydrot. Energy* **2017**, *42*, 2257–2264.
15. Young, K.; Ouchi, T.; Nei, J.; Koch, M.J.; Lien, Y. Comparison among constituent phases in superlattice metal hydride alloys for battery applications. *Batteries* **2017**, submitted.
16. Young, K.; Huang, B.; Regmi, R.K.; Lawes, G.; Liu, Y. Comparisons of metallic clusters imbedded in the surface of AB_2 , AB_5 , and A_2B_7 alloys. *J. Alloy. Compd.* **2010**, *506*, 831–840.
17. Young, K.; Chang, S.; Lin, X. C14 Laves phase metal hydride alloys for Ni/MH batteries applications. *Batteries* **2017**, accepted.
18. Young, K.; Ouchi, T.; Huang, B.; Reichman, B.; Fetcenko, M.A. The structure, hydrogen storage, and electrochemical properties of Fe-doped C14-predominating AB_2 metal hydride alloys. *Int. J. Hydrot. Energy* **2011**, *36*, 12296–12304.
19. Young, K.; Ouchi, T.; Reichman, B.; Koch, J.; Fetcenko, M.A. Improvement in the low-temperature performance of AB_5 metal hydride alloys by Fe-addition. *J. Alloy. Compd.* **2011**, *509*, 7611–7617.
20. Shinya, K.; Magari, Y.; Akita, H.; Kumagae, K.; Nakamura, H.; Matsuta, S.; Nohma, T.; Takee, M.; Ishiwa, K. Investigation into the deterioration in storage characteristics of nickel-metal hydride batteries during cycling. *J. Power Sources* **2005**, *143*, 265–269.
21. Teraoka, H. Development of Highly Durable and Long Life Ni-MH Batteries for Energy Storage Systems. In Proceedings of the 32th International Battery Seminar & Exhibit, Fort Lauderdale, FL, USA, 9–12 March 2015.
22. Young, K.; Yasuoka, S. Capacity degradation mechanisms in nickel/metal hydride batteries. *Batteries* **2016**, *2*, 3. [[CrossRef](#)]
23. Meng, T.; Young, K.; Koch, J.; Ouchi, T.; Yasuoka, S. Failure mechanisms of nickel/metal hydride batteries with cobalt-substituted superlattice hydrogen-absorbing alloy anodes at 50 °C. *Batteries* **2016**, *2*, 20. [[CrossRef](#)]

24. Yasuoka, S.; Ishida, J.; Kai, T.; Kajiwara, T.; Doi, S.; Yamazaki, T.; Kishida, K.; Inui, H. Function of aluminum in crystal structure of rare Earth-Mg-Ni hydrogen-absorbing alloy and deterioration mechanism of Nd_{0.9}Mg_{0.1}Ni_{3.5} and Nd_{0.9}Mg_{0.1}Ni_{3.3}Al_{0.2} alloys. *Int. J. Hydrot. Energy* **2017**, *42*, 11574–11583.
25. Young, K.; Wang, L.; Yan, S.; Liao, X.; Meng, T.; Shen, H.; Mays, W.C. Fabrications of high-capacity alpha-Ni(OH)₂. *Batteries* **2017**, *3*, 6. [CrossRef]
26. Singh, D. Characteristics and effects of γ -NiOOH on cell performance and a method to quantify it in nickel electrode. *J. Electrochem. Soc.* **1998**, *145*, 116–120.
27. Yuan, A.; Cheng, S.; Zhang, J.; Cao, C. Effects of metallic cobalt addition on the performance of pasted nickel electrodes. *J. Power Sources* **1999**, *77*, 178–182.
28. Jayashree, R.S.; Kamath, P.V. Suppression of the α -nickel hydroxide transformation in concentrated alkali: Role of dissolved cations. *J. Appl. Electrochem.* **2001**, *31*, 1315–1320.
29. Tessier, C.; Guerlou-Demouragues, L.; Faure, C.; Denage, C.; Delatouche, B.; Delmas, C. Influence of zinc on the stability of the β (II)/ β (III) nickel hydroxide system during electrochemical cycling. *J. Power Sources* **2001**, *102*, 105–111.
30. Ravikumar, C.R.; Kotteeswaran, P.; Bheema Raju, V.; Murugan, A.; Santosh, M.S.; Nagaswarupa, H.P.; Prashantha, S.C.; Anil Kumar, M.R.; Shivakumar, M.S. Influence of zinc additive and pH on the electrochemical activities of β -nickel hydroxide materials and its applications in secondary batteries. *J. Energy Storage* **2017**, *9*, 12–24.
31. Zhou, X.; Young, K.; West, J.; Regalado, J.; Cherisol, K. Degradation mechanisms of high-energy bipolar nickel metal hydride battery with AB₅ and A₂B₇ alloys. *J. Alloy. Compd.* **2013**, *560*, S373–S377.
32. Young, K.; Ouchi, T.; Koch, J.; Fetcenko, M.A. Compositional optimization of vanadium-free hypo-stoichiometric AB₂ metal hydride alloy for Ni/MH battery application. *J. Alloy. Compd.* **2012**, *510*, 97–106.
33. Young, K.; Ouchi, T.; Fetcenko, M.A. Pressure-composition-temperature hysteresis in C14 Laves phase alloys—Part 1 Simple ternary alloys. *J. Alloy. Compd.* **2009**, *480*, 428–433.



© 2017 by the authors. Licensee MDPI, Basel, Switzerland. This article is an open access article distributed under the terms and conditions of the Creative Commons Attribution (CC BY) license (<http://creativecommons.org/licenses/by/4.0/>).